INORGANIC CHEMISTRY FRONTIERS

RESEARCH ARTICLE

View Article Online
View Journal | View Issue



Cite this: *Inorg. Chem. Front.*, 2023, **10**, 3047

# Medium-entropy state quinary keplerate clusters as a remarkable electrocatalyst for small molecule electrooxidation†

Mengyang Cao,‡ Hongfang Ye,‡ Yingying Liu, Jianwen Wang, Yin Zhou, Xianwen Wang, Shining Wu, Feng Xu * and Yingpeng Wu *

Received 18th February 2023,
Accepted 4th April 2023

DOI: 10.1039/d3qi00316g

rsc.li/frontiers-inorganic

The synthesis of discrete polyoxometalate clusters composed of more than 3 metallic elements has always been attractive but seldom successful. For the first time, we have developed a *de novo* synthetic route to quinary Cu–Ni–Co–Mn–Zn Keplerate clusters with a nuclearity of 20. Seven single-crystalline quinary Keplerates in a medium-entropy state with various compositions have been obtained. A systematic study reveals that the different ions' ability to be incorporated into the Keplerates is governed by the Irving–Williams series, and they are stabilized in a medium entropy state. More intriguingly, these quinary Keplerate clusters represent an analogue of the Ship of Theseus at the molecular level, *i.e.*, the global features of the $\{M_{20}\}$ Keplerates are intact, while the constitution can be altered by tuning the synthesis conditions. Our further investigation reveals that the quinary elements $\{M_{20}\}$ compared to mono-component and binary Keplerate clusters exhibit much superior electrochemical performance, therefore shedding light on the design of multimetallic clusters in high-entropy states as novel electrocatalysts.



## 1. Introduction

Polyoxometalates (POMs), comprising multiple transition metal centers in different oxidation states, are among the most attractive inorganic redox active materials for numerous applications such as energy conversion, catalysis and chemical sensing.[1–3] Currently, it is of great interest to fabricate discrete POM clusters composed of more than 3 metal elements, since the inherent features of POMs such as the substitutability of the metal centers[4] or high active site density can be combined with the improved catalytic performance derived from the configurational tunability and compositional diversities of various metal elements.[5] However, it is still hard to confine more than 3 metal elements in the assembly of single-phase POM clusters. This aim is subjected to the incompatibility of various metal atoms and unpredictable combinations in the solution environment. Not only the thermodynamic high mixing enthalpy but also the atomic size difference and complex atomic arrangement impede the controllable multi-component system accessibility.[6] In the synthesis of multimetallic materials, extreme synthesis conditions are necessary to overcome the challenges above. For example, it has been reported that the fabrication of a high entropy alloy, one of the most promising multimetallic materials, requires an extreme local environment, such as high temperature shock (~2000 K, ~$10^5$ K per second) or ball milling,[7,8] thus multicomponent cluster synthesis has rarely been achieved.[9,10] Besides the harsh conditions, this strategy cannot be applied to the synthesis of multimetallic POMs, mainly because these conditions would lead to metal oxides rather than discrete POM clusters. Hence, it is paramount to identify appropriate candidates from the library of POMs, with the ultimate aim of synthesizing multimetallic materials in a flexible and controllable fashion.

Polyoxocuprates (POCus) are an emerging class of POM-like architectures.[11] It has been clearly demonstrated that at least two different metal elements can be incorporated into the $\{M_{20}\}$ skeletons of the Keplerates,[12] which makes them a promising candidate as a versatile platform in studying multimetallic clusters.[11] Consequently, we are prompted to investigate whether four other 3D metal elements (Co, Ni, Zn and Mn) could be simultaneously incorporated into the $\{Cu_{20}\}$ Keplerate with high symmetry by following the low-cost and facile synthesis of $\{Cu_{20}\}$.[12–15]

Herein, we report a *de novo* synthetic route to quinary $\{M_{20}\}$ Keplerate clusters containing Cu, Ni, Co, Mn and Zn. Seven single-crystalline quinary Keplerates (named M20-20 to M20-26) in a medium-entropy state with various compositions have

*State Key Laboratory of Chem/Bio-Sensing and Chemometrics, Advanced Catalytic Engineering Research Center of the Ministry of Education, College of Chemistry and Chemical Engineering, Hunan University, Changsha, 410082, P. R. China.*
*E-mail: wuyingpeng@hnu.edu.cn, feng_xu@hnu.edu.cn*

†Electronic supplementary information (ESI) available. CCDC 1471374 (M20-7), 1840132 (M20-17) and 1840131 (M20-24). See DOI: https://doi.org/10.1039/d3qi00316g

‡These authors contributed equally to this paper.

been obtained and characterized. Through our systematic studies, we demonstrate that the different ions' ability to be incorporated into the $\{M_{20}\}$ Keplerates is governed by the Irving–Williams series. Furthermore, we show that one of the quinary Keplerates of the $\{M_{20}\}$ library M20-20, with the metal composition $Cu_{12.87}Ni_{2.93}Co_{2.88}Zn_{1.12}Mn_{0.18}$, as representative of the multimetallic clusters, exhibits much superior performance with a current density of 280.1 mA $cm^{-2}$ at 0.8 V (Ag/AgCl) for methanol electrooxidation (MOR) and sensitivity of 2.99 mA $mM^{-1}$ $cm^{-2}$ for glucose detection. The binary cluster achieves significant improvement as compared with the monocomponent and binary $\{M_{20}\}$. Additionally, to the best of our knowledge, this is the best MOR performance in non-noble POMs. The morphological and componential evolution of M20-20 after electrochemical reaction was revealed to exhibit potential for multicomponent material synthesis.

## 2. Experimental

### 2.1 General synthesis procedures of $\{M_{20}\}$ library clusters

Detailed descriptions for the synthesis of each cluster (M20-7, M20-9, M20-10, M20-17, M20-19, M20-20 to M20-26) in the $\{M_{20}\}$ library are provided in the ESI†: $\{M_{20}\}$ Library Synthesis Details. Here is a general protocol. (a) Before the synthesis, metal acetates were mixed in 20 mL of $CH_3CN$ with 2 mL of iso-propylamine and 400 μL of $H_2O$. (b) The mixture was stirred for 24 h in an ambient environment to dissolve the metal acetates; another 10 mL of methanol was added to dissolve if a gel emerged. (c) The clear solution was then filtered and evaporated for a few days to obtain the single crystal for later characterization. Notably, when inferior single crystals are produced, recrystallization by methanol is of necessity (repeated multiple times if needed).

### 2.2 Synthesis of NCNT, NCNT-M20-20 1 : 1, NCNT-M20-20 2 : 1, NCNT-M20-20 3 : 1, CNT-$Cu_{20}$, M20-CuNi and M20-CuCo

Acidized multiwalled carbon nanotubes (MWCNT) were synthesized through the solvothermal method: 0.12 g of MWCNT was added to 50 mL of mixed solvent with a volume ratio of $HNO_3$ (concentrated) : $H_2O$ of 1 : 3 for 14 h at 160 °C. The acidized MWCNT was rinsed with distilled water three times to remove the residual acid and then freeze-dried to obtain the porous products. The nitrogen doped multiwalled carbon nanotubes (NCNT) were prepared by mixing melamine and acidized MWCNT with a mass ratio of melamine : MWCNT (acidized) of 3 : 1 through mechanical mixing followed by calcination under an Ar atmosphere at 700 °C for 1 h.

Mixing NCNT with M20-20 at different mass ratios of 1 : 1, 2 : 1 and 3 : 1 (the ratio is 1 : 1 for NCNT-$Cu_{20}$) in ethanol and stirring for 36 h, then evaporating at room temperature in a vacuum oven provided the final products NCNT-M20-20 1 : 1, NCNT-M20-20 2 : 1, NCNT-M20-20 3 : 1 and NCNT-$Cu_{20}$.

M20-CuCo/M20-CuNi was prepared with M20-10/M20-7 and NCNT in the mass ratio of NCNT : M20-10/M20-7 of 2 : 1, and the other conditions were the same as for NCNT-M20-20 2 : 1.

### 2.3 Chemicals and characterization procedures

All of the reactants were purchased from Shanghai Aladdin Co. Ltd at reagent grade and used without pre-treatment. The multi-walled carbon nanotubes were purchased from SuZhou TANFENG graphene Tech Co., Ltd.

IR spectra were measured on a WQF-410 FT-IR spectrometer. UV-Vis absorption spectra were obtained using a 752 PC UV-Vis spectrophotometer. Thermogravimetric analysis (TGA) measurements were carried out using a DSC/TG pan A1203 system with an $N_2$ flow with a heating rate of 5 °C $min^{-1}$. Elemental analyses (C, H, N) were performed using a Thermo Scientific FLASH 2000 elemental analyzer; Cu, Co, Ni, Zn and Mn were analyzed on a Varian (720) ICP atomic emission spectrometer. The morphology and EDS of all the materials were investigated using a scanning electron microscope (SEM, Hitachi, S-4800). Powder X-ray diffraction results were from a Bruker D8 ADVANCE, Cu Kα1 ($\lambda$ = 0.15418 nm, 2$\theta$ range from 10 to 90°). X-ray photoelectron spectroscopy tests used a Thermo SCIENTIFIC ESCALAB 250 photoelectron spectrometer with Al Kα as the excitation source. Single-crystal X-ray analyses were performed at room temperature on a Siemens SMART platform diffractometer outfitted with an Apex II area detector and monochromatized MoKα radiation ($\lambda$ = 0.71073 Å). Structures were solved by direct methods and refined using the SHELXTL software package.[16] All electrochemical measurements were made using a CHI 760E (Chen Hua Instruments Co. Ltd, Shanghai).

The electrochemical characterization of the NCNT-M20-20 1 : 1, NCNT-M20-20 2 : 1, NCNT-M20-20 3 : 1, M20-CuNi, M20-CuCo and NCNT-$Cu_{20}$ composites was conducted in a conventional three electrode cell on a CHI760E electrochemical workstation (Shanghai Chenhua Instrument Co., China). The catalyst slurry was made by mixing 3 mg of the composite with 30 μL of Nafion solution, 170 μL of ultrapure water and 800 μL of ethanol, and sonicating for 5 min. The working electrode was prepared by dropping 15 μL of the catalyst slurry on a glassy carbon electrode (GCE) and drying naturally. The catalyst loaded GCE acted as the working electrode, Ag/AgCl (3.5M KCl) as the reference electrode, and a Pt plate as the counter electrode. The tests were performed in 1M KOH, and methanol was added to the electrolyte to examine the MOR ability. Before the CV test, several CV cycles were conducted on the electrode for stabilization. All cures were tested without IR compensation. 0.4 V was chosen as the working potential when conducting the electrochemical impedance spectroscopy (EIS) at frequencies ranging from 10 kHz to 0.1 Hz with an AC perturbation of 10 mV in 1 M KOH. Chronoamperometry was conducted at 0.7 V for 6 h to test the stability.

## 3. Results and discussion

### 3.1. $\{M_{20}\}$ library discovery

Inspired by our previous work in which 20 metal center polynuclear $\{Cu_{20}\}$ species and the Cu–Zn bimetallic analogue ($\{Cu_{12}Zn_8\}$) were discovered,[17] we first started the multicompo-

 

nent cluster synthesis with Cu–Ni and Cu–Co bimetallic icosanuclear clusters (*i.e.* M20-7 and M20-9, see Table S1†). A general procedure to obtain $\{M_{20}\}$ counterparts is shown in Fig. 1a as an intuitive demonstration. According to the XRD results (Fig. 1b and c), bimetallic clusters M20-7 (Cu–Ni) and M20-9 (Cu–Co) share nearly the same pattern as the reported

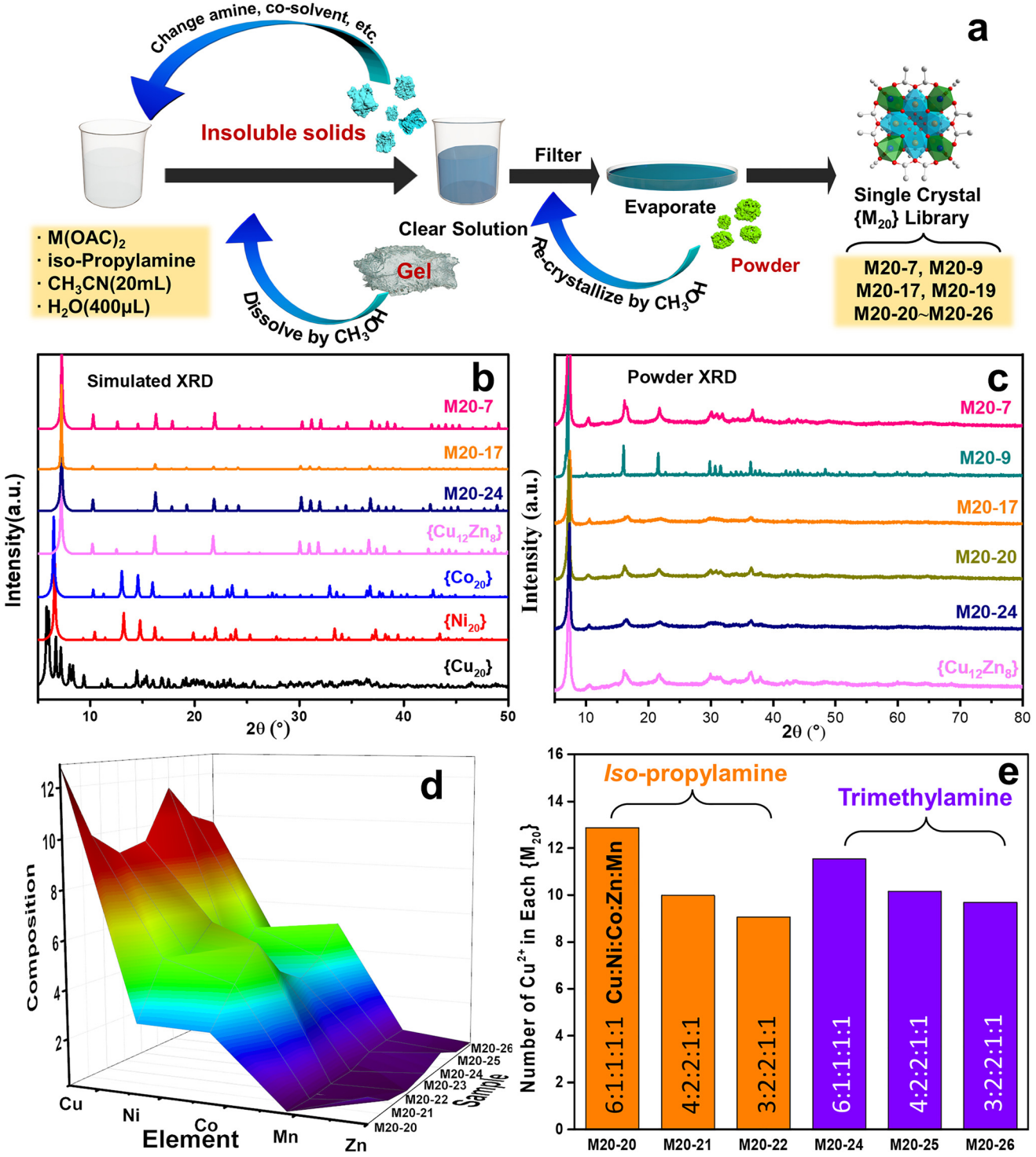


**Fig. 1** Synthesis and structural characterizations of clusters. (a) Illustration of the *de novo* synthetic route of $\{M_{20}\}$ Keplerate clusters. (b) Simulated powder XRD patterns of M20-24, M20-7, M20-17, $\{Cu_{12}Zn_8\}$, $\{Ni_{20}\}$, $\{Co_{20}\}$ and $\{Cu_{20}\}$ based on single crystal data. (c) Powder XRD of M20-7, M20-9, M20-17, M20-20, M20-24 and $\{Cu_{12}Zn_8\}$. (d) A surface plot of the relationship between metal compositions and elements in the quinary systems (M20-20 to M20-26), indicating that the number of metal elements in the $\{M_{20}\}$ series is governed by the Irving–Williams series. (e) Bar chart to illustrate the influence of the starting salt molar ratio and amine on the number of $Cu^{2+}$ in $\{M_{20}\}$. The ratio inside each bar is the salt molar ratio $Cu^{2+}:Ni^{2+}:Co^{2+}:Zn^{2+}:Mn^{2+}$.

$\{Cu_{12}Zn_8\}$. Considering the possible extension to more complicated multimetallic Keplerates, the result led to further attempts. Five divalent metal ions ($Cu^{2+}$, $Co^{2+}$, $Ni^{2+}$, $Zn^{2+}$, $Mn^{2+}$) were mixed, and the solution products were subsequently obtained as shown in Fig. S1.† After the crystallization, the quinary element product M20-20 (Cu–Ni–Co–Zn–Mn) was synthesized. The presence of all five metal elements in the M20-20 was confirmed by EDS and ICP results, as displayed in Fig. 2b and Table S1.† The amine and transition metal salts were diversified to produce other counterparts M20-21 to M20-26. Subtle alteration of the synthetic parameters was necessary to achieve the successful synthesis of different counterparts. All the attempts to expand $\{M_{20}\}$ are exhibited in Table S2.† The obtained binary M20-7 (Cu–Ni), M20-9 (Cu–Co) and M20-10 (Cu–Co), ternary M20-17 (Cu–Ni–Co), and quaternary M20-19 (Cu–Ni–Co–Zn), together with quinary M20-20 to M20-26 (Cu–Ni–Co–Zn–Mn) constitute the $\{M_{20}\}$ library. During the extension from binary clusters to the $\{M_{20}\}$ library we found the clusters maintained Keplerate structure even with increasing complexity and species diversity in solution. Detailed descriptions are given in part 3.2: Purity and structure analysis. A general ball-and-stick model of $\{M_{20}\}$ is presented in Fig. S2b;† crystallographic data and structure refinement of the synthesized M20-7, M20-17 and M20-24 are present in Table S5.†

### 3.2. Purity and structure analysis

The powder and single crystal XRD results were examined to ensure the as-obtained multimetallic samples were not mixtures of their monometallic clusters like $\{Cu_{20}\}$, $\{Co_{20}\}$ and $\{Ni_{20}\}$. Fig. 1b displays the simulated powder XRD patterns based on the single-crystal structure data of $\{Cu_{20}\}$, $\{Co_{20}\}$, $\{Ni_{20}\}$, $\{Cu_{12}Zn_8\}$, M20-7, M20-17 and M20-24.[17,18] Evidently, the patterns of M20-7 (Cu–Ni), M20-17 (Cu–Ni–Co) and M20-24 (Cu–Ni–Co–Zn–Mn) show great resemblance with the $\{Cu_{12}Zn_8\}$ Keplerate structure, while sharing little in common with $\{Cu_{20}\}$, $\{Co_{20}\}$ and $\{Ni_{20}\}$. The similar patterns indicate M20-7, M20-17 and M20-24 have the same Keplerate structure as $\{Cu_{12}Zn_8\}$. In addition, the powder XRD results of M20-7, M20-17 and M20-24 (Fig. 1c) match closely the simulated patterns, suggesting the synthesized products are of high purity. The XRD pattern similarity of binary (M20-7, M20-9) and quinary (M20-24) Keplerates indicates that the crystal skeleton remains the same, despite the number of TM elements increasing from two to five. Furthermore, when the molar ratio of the salt precursor and amine was changed in the synthesis

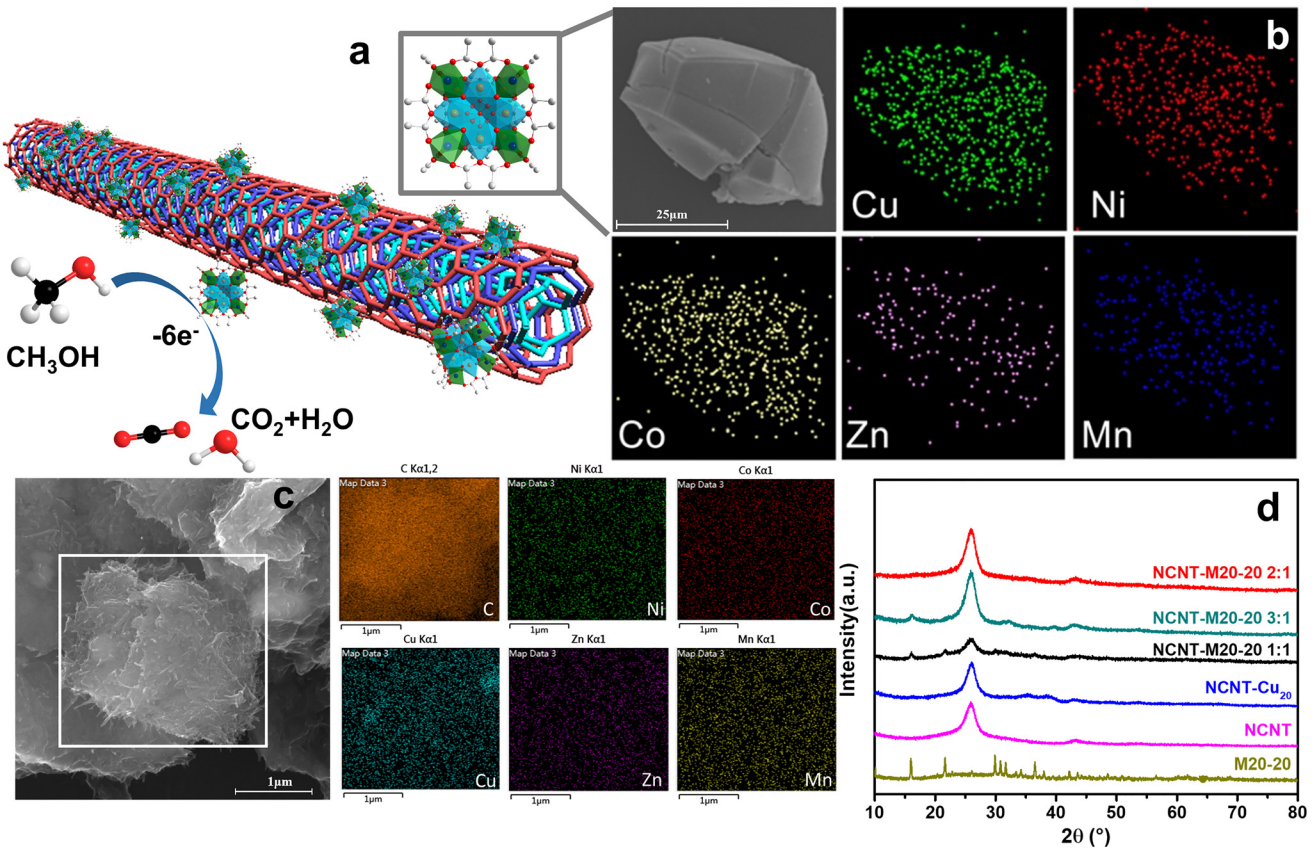


Fig. 2 Structural characterizations of the NCNT-M20-20 composite. (a) Graphic illustration of NCNT-M20-20 2 : 1 in the MOR process, with the structure of M20-20 shown as a ball-stick model. (b) Morphology of M20-20 and mapping information of the selected area. (c) Morphology of NCNT-M20-20 2 : 1 and EDS results. (d) Powder XRD of a series of materials.

 

conditions, the crystal skeleton of the obtained product also remained constant. Specifically, M20-20 and M20-24, which were synthesized with various amines and precursor ratios, have similar XRD patterns. The constant crystal skeleton and substitutable cations of the POM-based $\{M_{20}\}$ library suggests an analogue of the ship of Theseus at the molecule level. A similar situation is found for metal–organic frameworks (MOF) in which Zn is replaced by Ni.[19] Control experiments to obtain monometallic $\{Co_{20}\}$, $\{Ni_{20}\}$, $\{Zn_{20}\}$ and $\{Mn_{20}\}$ have failed, thus further excluding the likelihood of their mixtures featuring in the $\{M_{20}\}$ library. Unexpectedly in control experiments, two homometallic compounds $\{Ni_9\}$ and $\{Mn_{25}\}$ were obtained, exhibiting similar structures to the compounds in previous literature.[20] Fig. S3† shows the structure of the $\{Ni_9\}$ cluster. The fact that $\{Ni_9\}$ was obtained rather than $\{Ni_{20}\}$ indicates that the method to synthesize the $\{M_{20}\}$ library here cannot lead to the formation of $\{Ni_{20}\}$ and therefore the possibility of mixed monocomponent clusters in the $\{M_{20}\}$ library is further excluded. The IR spectroscopy and TGA results of M20-7, M20-17 and M20-20 are collected in Fig. S4 and S5 with Note S1† as the supplementary evidence of high similarity.

### 3.3. Structure features of the $\{M_{20}\}$ library: medium entropy state and following the Irving–Williams series

To better describe and understand the $\{M_{20}\}$ library, another concern followed: whether all metal sites in the samples can be defined precisely like the reported $\{Cu_{12}M_8\}$ (M = Cu, Zn, La, Mg) with a certain atom ratio? Speculating as a result of the high similarity XRD patterns, we first assumed that $\{M_{20}\}$ counterparts, similar to $\{Cu_{12}M_8\}$, exhibit a specific element ratio derived from the highly symmetric character of Keplerates. X-ray diffraction has its limitations in accurately defining the metal site because of the similarity of the atomic masses of close elements, together with the intrinsic high symmetry of $\{M_{20}\}$. ICP characterization was coupled to eliminate this concern, and $\{M_{20}\}$ counterparts featuring non-integer ratios were uncovered as summarized in Table S1.† Unexpectedly, none of M20-20 to M20-26 have a certain integral mole fraction. The ICP results show that the structure of $\{M_{20}\}$ features neither typical well-crystallized Keplerates nor ordered intermetallics. The disorderliness of the elements suggests the character of a single-phase state with random distributions is similar to HEA. According to the previous literature,[21] the formation of single-phase HEA requires higher mixing entropic change than mixing enthalpic ones to realize a negative Gibbs free energy change. For the quinary system, elements that fail to be miscible with each other will cause a positive Gibbs free energy change and thus phase separation. M20-20 to M20-26 were verified to be single-phase by single-crystal structure data of M20-24. Additionally, the EDS showed that the elements are also evenly distributed (Fig. 2b), thereby the quinary $\{M_{20}\}$ are entropy-stabilized to a stable single-phase. The mixing entropy is calculated for M20-20 according to the equation below:[22]

$$\Delta S_{\mathrm{mix}} = -R \sum x_i \ln x_i$$

$R$ is the gas constant and $x_i$ is the mole ratio of the $i$ component. The contribution of the anion sites is not considered because of the minor effect on the entropic contribution. The $\Delta S_{\mathrm{mix}}$ of M20-20 is calculated to be $1.04R$, which falls into the category of medium entropy range.[22] From the results so far, it is clear that metal elements in the quinary $\{M_{20}\}$ are entropy driven stabilized and randomly distributed. The lattice distortion caused by the random distribution of atoms in the high entropy state also leads to a weak XRD intensity[23] for M20-17, M20-20 and M20-24 compared with the binary clusters M20-7 and M20-9 in Fig. 1c. Besides the quantity of the elements, XPS was used to illustrate the valence states of the clusters. Fig. S6–S9† demonstrate the XPS results of M20-20, M20-17, M20-7 and M20-9. According to the results, all elements of the single crystals are at +2 valence. This is similar to the formation of some types of high entropy oxides that share the same oxidation state such as cubic rock-salt multi-cation oxide.[21] The effort to expand the Keplerate $\{M_{20}\}$ to $Fe^{2+}$ has failed. We assumed the valence state could affect $\{M_{20}\}$ formation, and $Fe^{2+}$ is inclined to be oxidized to +3 in an oxygen-containing ambient environment, thus the additional charge will break the electroneutrality, finally resulting in structural collapse of the Keplerate structure.

Investigations into the compositions by ICP lead to further insights regarding the complex molecular assembly of the $\{M_{20}\}$ Keplerates. Initially, the ICP analysis of M20-24 obtained in different batches was performed three times to verify the ICP data and method repeatability (Table S3†). When all counterparts were summarized in tables (Table S1†), we noticed that the abilities of the bivalent cations to be incorporated into the Keplerates were different. This exactly follows the Irving–Williams trend where the relative stabilities of complexes formed by transition metals are in the order $Mn^{2+} < Co^{2+} < Ni^{2+} < Cu^{2+} > Zn^{2+}$.[24] Specifically, with equivalent amounts of starting metal salts, the mole ratio of the product (M20-23) is consistent with this trend as Cu : Ni : Co : Zn : Mn = 9.37 : 6.01 : 4.10 : 0.39 : 0.13. The results of products with equivalent or element-equivalent amounts of starting metal salts are compared in Table S4.† The tendency from the ICP results confirms that the proportion of each element agrees with the Irving–Williams Series. In other words, inside the $\{M_{20}\}$ Keplerates, the divalent cation proportion increases with the intrinsic stability. For a better illustration of elements and metal compositions, the underlying trend among M20-20 to M20-26 is plotted in Fig. 1d. It can be seen that there is a clear downtrend from Cu to Zn. So far, we know the cations in $\{M_{20}\}$ are stabilized in a medium entropy state and according to the intrinsic stabilities of the Irving–Williams series to form the clusters in different proportions.

### 3.4. Influence of precursor ratio and solvent on the products

We attempted to investigate the influence of the precursor salt ratio and solvent on the products. As shown in Fig. 1e, the products synthesized with different amines and precursor salt ratios are divided into two groups. It can be seen that Cu species are more easily assembled with a high $Cu^{2+}$ proportion

(>10) in iso-propylamine than in trimethylamine when comparing M20-20 with M20-24 at equal precursor ratios. In contrast, for low amounts of $Cu^{2+}$ (<10), the $Cu^{2+}$ amount is higher in trimethylamine than in iso-propylamine, as shown with M20-21/M20-25 and M20-22/M20-26. Trimethylamine from a thermodynamics viewpoint may not be as favorable as iso-propylamine for Cu species to assemble clusters in an environment with high proportions of copper, but it is more favorable in environments with low copper proportions. Elements exhibit different equilibria in different solutions and result in the same structures, and diverse proportions prove the thermodynamic stability of the Keplerate structure. However, in contrast to the quinary system, the high copper proportion will lead to the failure of the formation of binary to quaternary Keplerates as exhibited in Table S2.† In the trials to produce Cu–Co, Cu–Ni–Zn, Cu–Co–Zn, Cu–Ni–Co and Cu–Ni–Co–Zn counterparts, high copper precursor ratios of 5 : 2 : 2 and 4 : 2 : 2 were applied, but only two counterparts were successfully synthesized. This illustrates that the copper precursor ratio is critical for the design and fabrication of different systems. The adjustable constituents show the potential programable regulation of the target Keplerate by using different synthesis conditions.

### 3.5. Electrochemical methanol oxidation

As a good electron reservoir in multiple electron transfer processes, POMs serve well in electrochemistry.[25–27] The multicomponent system combines every virtue of the components, offering appealing properties as a result of tailored electronic properties and compositional diversities.[28–30] Here, M20-20 as a typical quinary element compound was chosen as the test species for methanol and glucose electrooxidation catalysis to demonstrate the potential of the $\{M_{20}\}$ series and multicomponent system. To maximize the performance, nitrogen-doped multiwalled carbon nanotubes (NCNT) were used to anchor the M20-20 by electrostatic force to avoid the intrinsic poor electroconductivity of the single crystal (Fig. S10a and b†). The final product was named NCNT-M20-20. The mass ratio of M20-20 and NCNT was optimized from 1 : 1, 1 : 2 and 1 : 3. Fig. 2a shows a scheme of the composite MOR process. The uniform dispersion of five elements before and after the combination with NCNT was confirmed by the EDS test as shown in Fig. 2b and c. After the blending of the materials, the XRD shows characteristic peaks of both CNT and M20-20 (Fig. 2d).[31] The M20-20 peaks were weakened after mixing mainly due to the good dispersion and electrostatic force.

Cyclic voltammetry (CV) was applied to probe the methanol electro-oxidation ability of NCNT-M20-20. Fig. 3a shows the CV of NCNT-M20-20 2 : 1 in 1 M KOH with and without 0.5 M methanol. After the addition of methanol, the current density showed an apparent increase, indicating the high catalytic performance towards methanol; the double-step chronoamperometry also confirms that the current originated from methanol oxidation as discussed in the ESI Note S2.† There is a 235 mV advance because of the more preferential dynamics of MOR than OER as shown in the inset graph. At 0.8 V, the current density reaches 280.1 mA $cm^{-2}$, which suggests superior oxidation performance. When transferred to mass activity it also reaches as high as 281.5 mA $mg^{-1}$. A CV comparison is shown in Fig. S11a,† and among the four catalysts, NCNT-M20-20 2 : 1 shows the best activity. $\{Cu_{20}\}$, as a single metal cluster, exhibits a poor activity for methanol oxidation. Fig. 3b shows a great activity gap between NCNT-$Cu_{20}$ and NCNT-M20-20 2 : 1, although their electric double layer capacitance ($C_{dl}$) (inset graph) is at the same level. The results above demonstrate that the multicomponent system gives the material a significant property enhancement because of the so-called "cocktail effect".[32] When subtracting the baseline current originating from the CV of the OER process, the current density at 0.8 V shows a high specific activity of 179.3 mA $cm^{-2}$. The performances of non-noble materials in previous literature are compared in Table S6.† Considering that non-noble POM materials are rarely reported for MOR, the performance of our work can be regarded as a reference for non-noble POMs in the methanol electrooxidation field.

To investigate the intrinsic electrochemistry properties, CV without methanol was used to evaluate the electrochemical behavior of NCNT-M20-20 2 : 1. As demonstrated in Fig. S12b,† the oxidation and reduction peak current of NCNT-M20-20 2 : 1 is the highest among the catalysts, suggesting the most active sites. This conclusion is also supported by the $Ni^{3+}$ surface coverage active sites calculation in Note S3.† According to the previous studies, a higher oxidation peak current for NCNT-M20-20 2 : 1 can be partly ascribed to the larger surface coverage of redox species.[33] The CV technique was further used to study the electrochemical species behavior and it verified that the transformation of $Ni^{3+}$–$Ni^{2+}$ redox process is a surface-controlled process.[34] Further discussions are listed in Note S4.† Chronoamperometry was conducted at 0.7 V to test the stability during the MOR process. As demonstrated in Fig. 3d, NCNT-$Cu_{20}$ (black line) rarely has MOR activity. For NCNT-M20-20 2 : 1 there is an apparent oxidation current at 0.7 V. After 6 h, the current density remains 24 mA $cm^{-2}$. Electrochemical impedance spectroscopy (EIS) measurements were carried out to get insights into the charge transfer process. In Nyquist plots of all the samples, NCNT-M20-20 2 : 1 shows the smallest diameter of the semicircle, claiming the lowest charge transfer resistance as displayed in Fig. 3c.[35] NCNT-$Cu_{20}$ shows the largest diameter with an $R_{ct}$ of 427.1 ohms, which is much larger than NCNT : M20-20 2 : 1 (29.69 ohms), NCNT : M20-20 1 : 1 (192.5 ohms) and NCNT : M20-20 3 : 1 (144.5 ohms). EIS results support the idea that a multielement composition reduces the charge transfer resistance, along with the NCNT together boosting the electron transfer between the catalyst and the methanol. The electrochemically active surface area (ECSA) of NCNT-M20-20 2 : 1 is 427.00 $cm^2$, which is the highest among the catalysts. NCNT-$Cu_{20}$ has the same level of ECSA (264.00 $cm^2$) as NCNT-M20-20 2 : 1, but exhibits poor performance (Note S5†), which hints at the importance of the multimetallic synergistic effect for the electrochemical process. When considering the high methanol concentration tolerance, it turns out that the NCNT-M20-20 2 : 1 is more stable than NCNT-$Cu_{20}$, as shown in Fig. S13,† because of the fast conversion of the intermediate to the final products. It has also been proved theoreti-

 

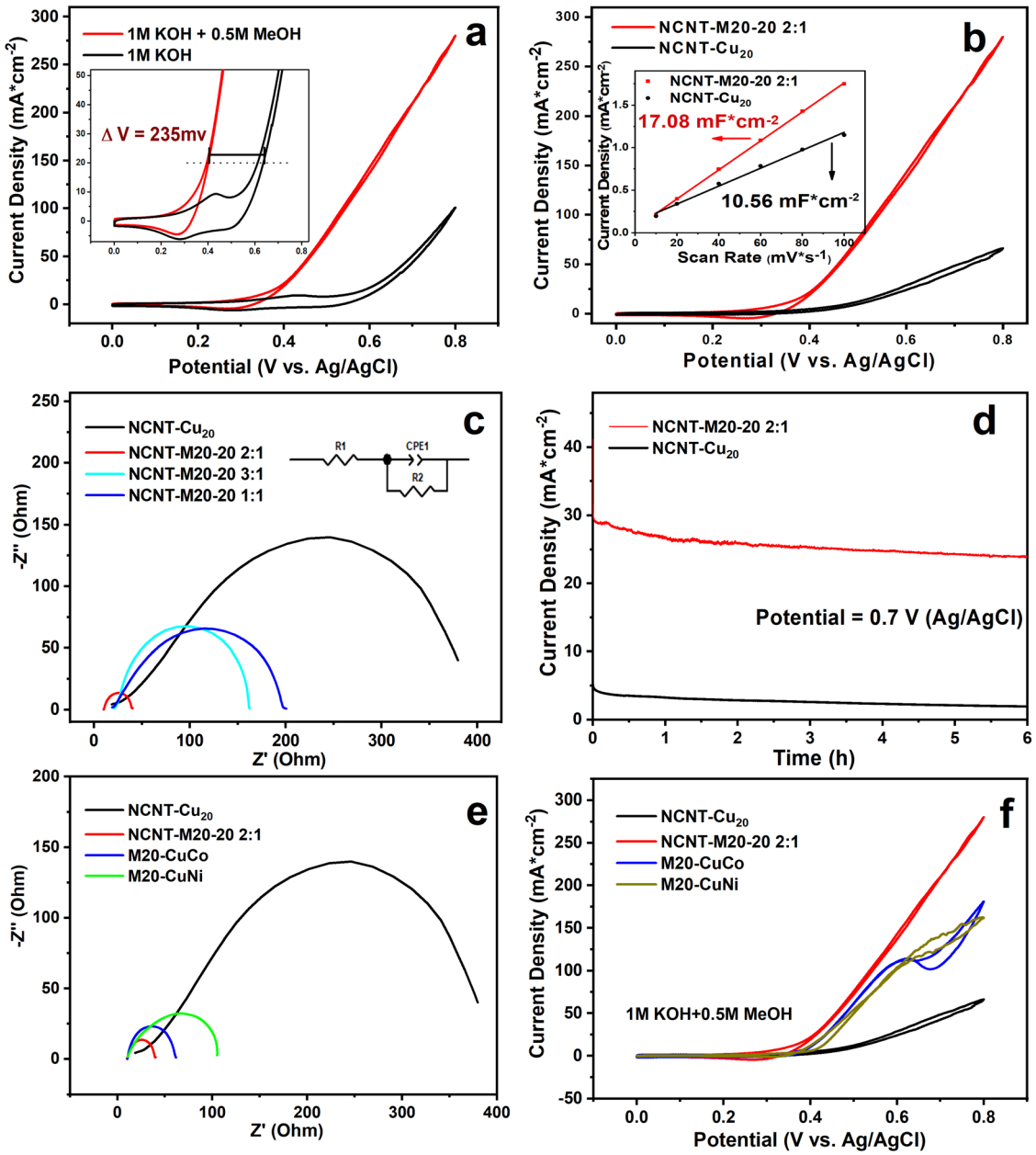


**Fig. 3** Electrochemical characterization of NCNT-M20-20 for the MOR process. (a) CV comparison of NCNT-M20-20 2 : 1 in 1 M KOH and 1 M KOH with 0.5 M methanol; the upper-left inset is an enlarged view. (b) CV curves of NCNT-M20-20 2 : 1 and NCNT-$Cu_{20}$ electrode in 1.0 M KOH + 0.5 M MeOH. The inset image shows the electric double-layer capacitance comparison of the two materials. (c) EIS test result of different samples. (d) NCNT-$Cu_{20}$ and NCNT-M20-20 2 : 1 *i*–*t* curves in 1 M KOH with 0.5 M methanol. (e) Electrochemical impedance spectroscopy comparison of NCNT-$Cu_{20}$, NCNT-M20-20 2 : 1, M20-CuNi and M20-CuCo. (f) CV comparison of NCNT-$Cu_{20}$, NCNT-M20-20 2 : 1, M20-CuNi and M20-CuCo.

cally and experimentally that $Cu^{2+}$ exhibits a superior ability to adsorb methanol molecules on account of the hybridized electronic structure.[36,37] More details are discussed in Note S5.†

### 3.6. The influence of component number on the electrochemical performance

More investigations were conducted to provide a clearer understanding of the structure–activity relationship. First, the Keplerate structure of $\{M_{20}\}$ counterparts was confirmed by Fig. S15† and Fig. 1c. So, the following study focuses on the influence of the elemental composition on the MOR performance by using clusters with different numbers of elements. Ni and Co have been widely applied and investigated as efficient non-noble metal catalysts for MOR.[38] Therefore, we intended to investigate binary clusters of these two elements as a starting point. The 20 nuclei cluster $\{M_{20}\}$ counterparts M20-CuNi (M20-7) and M20-CuCo (M20-10) (Table S2†) were selected and applied to discuss the structure–activity relationship. The M20-

CuNi and M20-CuCo were prepared using the same method as NCNT-M20-20 2 : 1. The test conditions were the same as those for NCNT-M20-20 2 : 1. The ICP results indicated that the element ratio of the clusters are: M20-CuNi ($Cu_{10.38}Ni_{9.62}$), and M20-CuCo ($Cu_{9.80}Co_{10.20}$). XRD results showed that M20-CuCo and M20-CuNi share the same structure as M20-20 in Fig. S15.† The electrochemistry analysis is discussed below.

1. Through the CV test, the clusters M20-CuNi and M20-CuCo were both confirmed to exhibit activity towards methanol oxidation as shown in Fig. S16a and b.† The CV demonstrates a similar activity of M20-CuNi and M20-CuCo to MOR (Fig. 3f). However, the double layer capacitance ($C_{dl}$) in Fig. S17† shows that M20-CuCo has the highest $C_{dl}$ and M20-CuNi has the lowest $C_{dl}$. Considering the similar proportion in the clusters of Ni/Co (M20-CuNi, Ni:48.1%; M20-CuCo, Co:51.0%), it is reasonable to conclude that the nickel component is more efficient than cobalt and other elements in the $\{M_{20}\}$ Keplerate clusters. Besides, according to the EIS results in Fig. 3e, the charge transfer resistance of M20-CuNi is larger than that of M20-CuCo, again proving that the activity of the Ni component is better than that of Co. As a consequence, the activity can be evaluated by the amount of Ni.

2. Nevertheless, the performance of M20-20 is much higher than that of M20-CuNi, while the proportion of Ni in M20-20 (14.6%) is much lower than that of M20-CuNi (48.1%) (Fig. 3f). Based on the discussion above, we can conclude that the advantages of the multicomponent species exceed the contribution of the nickel component alone.

3. Furthermore, considering the electron transfer resistance, monocomponent $\{Cu_{20}\}$ possesses the largest resistance, quinary M20-20 has the lowest and the binary M20-CuNi and M20-CuCo are in the middle (Fig. 3e). The trend is therefore $R$(monocomponent) > $R$(binary) > $R$(quinary). Therefore, the charge transfer resistance decreases with the increase of the component number of clusters. Because of the reasons above, we believe that the increase in cluster components is beneficial for the charge transfer and catalytic activity. Additionally, the component number has a positive influence on the activity.

In general, binary clusters M20-CuCo and M20-CuNi were harnessed to prove that: ① the nickel component is the most efficient element in the $\{M_{20}\}$ Keplerate clusters; ② the multicomponent character has more advantages for MOR performance than the single component character; ③ an increase in the number of components is beneficial to the charge transfer in the reaction.

### 3.7. Structure evolution of M20-20 under anodic potential

To test the post-reaction structural integrity, chronoamperometry was conducted at 0.7 V for long term testing on pristine M20-20 in 1M KOH + 0.5 M MeOH. XRD and EDS tests were performed after the chronoamperometry.

As shown in Fig. S18,† Cu was transferred to $Cu(OH)_2$, while the other elements were in amorphous states. In SEM and EDS tests (Fig. S19†), the M20-20 was morphologically transferred from the bulk initial crystal to nano-bundles and elements are still evenly distributed on the $Cu(OH)_2$. The structure eventually become four metal element doped $Cu(OH)_2$ nano-bundles. The transformation means that the structure of the M20-20 underwent an evolution under the harsh oxidation environment in strong alkaline solution, and when exposed to alkaline oxidic conditions $Cu^{2+}$ will become a hydroxide, which is reported in previous cases of Cu-based materials.[39–42] The structure evolution accompanied with the disappearance of Keplerate, as a result the surface ligand like acetic acid ligand will peel off from the cluster.

Theoretically, after the collapse of the Keplerate structure, the metal atoms inside would undergo atom rearrangement and thus phase separation, followed by the formation of metal oxides/hydroxides in a strong alkaline solution. However, after the reaction, we did not observe the phase separation in the EDS results or the formation of metal oxides/hydroxides except $Cu(OH)_2$. The elemental composition also remained almost unchanged upon comparing the EDS results of Fig. S19 with Fig. S20.† Therefore, the M20-20 Keplerate framework actually protects the homogeneity of other transition elements during the evolution process.

In summary, the pristine M20-20 underwent a structural evolution under the high anodic potential, resulting in a morphological self-construction from giant bulk crystal to nano-bundles. The elements are reserved without leaching and the medium entropy state maintained. The elements retain the homogeneity after evolution under the protection of the Keplerate framework. The characteristics of morphological self-construction and framework-supported element homogeneity are promising for the development of multicomponent and high entropy materials.

### 3.8. Glucose electrochemical detection

For a further illustration of the $\{M_{20}\}$ library as promising candidates for diverse applications, NCNT-M20-20 2 : 1 was then tested as a probe for non-enzymatic glucose detection. Different potentials were applied to screen out the modest potential to investigate the sensitivity and amperometric responses. As shown in Fig. S21a,† 0.4–0.7 V was chosen to conduct the amperometric response $i$–$t$ test. The results show that the corresponding slope increases with the potential increase. The slope for 0.6 V is the highest among the four potentials. When the potential reached 0.7 V, the linearity of the response current nearly vanished because the OER process took over the glucose oxidation. Based on these results, 0.6 V was set as the testing potential for the following characterization. The real-time amperometric response tests were then carried out by successive injection of gradient glucose to the solution from 2 μM to 0.75 mM (Fig. 4a). The oxidation current increases with injection of glucose at concentrations as low as 2 μM, which demonstrates the high detection activity towards glucose. Furthermore, the catalyst showed a fast response time of about 3.5 s (Fig. S21b†). The corresponding calibration curve calculated from $i$–$t$ parallel tests is displayed in Fig. 4b. The amperometric current showed a linear dependence on the total glucose concentration over the range from

 

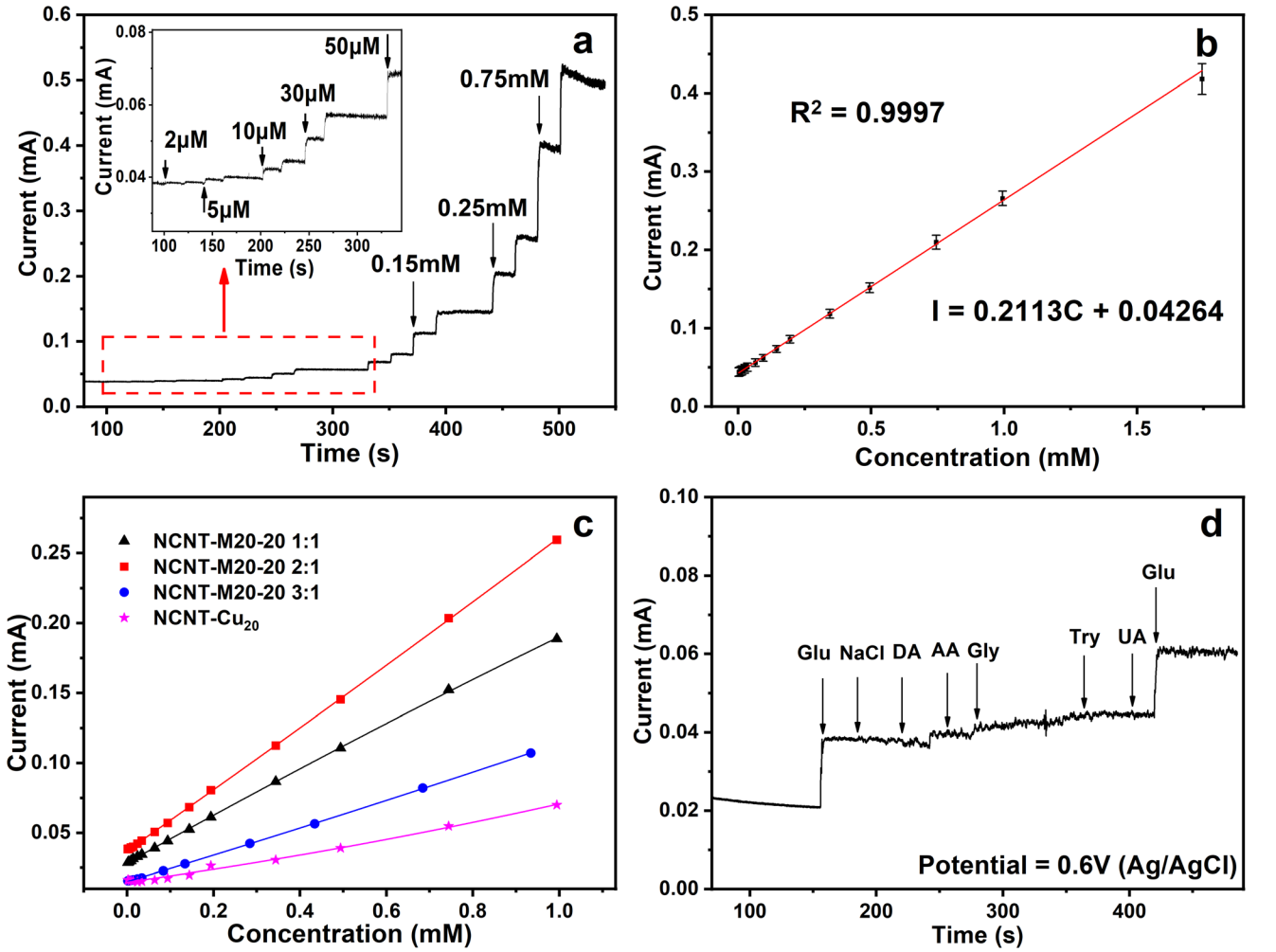


**Fig. 4** Electrochemical characterization of NCNT-M20-20 for the glucose detection process. (a) Amperometric response of NCNT-M20-20 2 : 1 with successive injections of increasing concentrations of glucose at 0.6 V. (b) The corresponding calibration curve of the current responses against the concentration of glucose. (c) The corresponding current-concentration calibration curves of all the samples. (d) Amperometric response of NCNT-M20-20 2 : 1 with continuous addition of glucose (0.1 mM), Glu (0.01 mM), NaCl (0.01 mM), DA (0.01 mM), AA (0.01 mM), Gly (0.01 mM), Try (0.01 mM), UA (0.01 mM) and again glucose (0.1 mM) at 0.6 V.

2 μM to 1.74 mM and the linear regression equation is calculated as:

$$I = 0.211C + 0.042 \ (R^2 = 0.9997)$$

where $I$ represents the response current and $C$ is the concentration of glucose. According to the equation, the sensitivity of the modified electrode is calculated to be 2.99 mA $mM^{-1}$ $cm^{-2}$, and the limit of detection (LOD) is 5.73 μM (S/N = 3). It is concluded that NCNT-M20-20 2 : 1 has the best performance among the counterparts as shown in Fig. 4c. The slope of the NCNT-M20-20 2 : 1 exhibits the best performance whereas NCNT-$Cu_{20}$ exhibits the lowest. This trend is consistent with the conclusion in the MOR performance test. The same result drawn from two applications implies that the multielemental interactions endow the catalysts with superior performance. Moreover, to explore the selectivity and anti-interference ability, possible interferences like NaCl, dopamine (DA), ascorbic acid (AA), glycine (Gly), tryptophan (Try) and uric acid (UA) were added successively in the presence of 0.1 mM of glucose to confirm the anti-interference ability. Fig. 4d displays the resulting *i*–*t* curve, and it can be seen that after the addition of these oxidizable substances, only a slight current increase was observed, indicating high selectivity towards glucose.

## 4. Conclusions

In summary, we demonstrated a general and mild method to synthesize Keplerate clusters containing up to five metallic elements and providing economic access to medium entropy materials. The studies on the synthesized single-crystalline Keplerates of various compositions were carried out systematically. Meanwhile, the underlying rules of the complex assembly of the Irving–Williams series and medium entropy state

were revealed by examining the composition of these new compounds. To show the possibility of application, one typical quinary compound, M20-20, was chosen as the catalyst and applied for methanol electrooxidation and glucose detection. The results showed promising performance as non-noble metal POMs. The comparison of binary and quinary $\{M_{20}\}$ shows the advantages of the multicomponent species, and the structure evolution of M20-20 under anodic potential was revealed. Our work opens up future possibilities for the mild directed synthesis of multimetallic ($\geq$5) polynuclear clusters with desired compositions and properties for electrochemistry applications.

## Author contributions

Conceptualization, supervision: Feng Xu and Yingpeng Wu; investigation, methodology: Hongfang Ye, Yingying Liu and Mengyang Cao; writing – original draft, writing – review & editing: Feng Xu, Yingpeng Wu and Mengyang Cao; validation: Jianwen Wang, Yin Zhou, Shining Wu and Xianwen Wang. All authors participated in the interpretation of the data and production of the final manuscript. Hongfang Ye and Mengyang Cao contributed equally.

## Data availability

The CIF files of synthesized clusters have been submitted to the Cambridge Crystallographic Data Centre (CCDC). M20-7: 1471374 (CCDC unpublished); M20-17: 1840132 (CCDC unpublished); M20-24: 1840131 (CCDC unpublished). Files of cif and check cif of M20-7, M20-17 and M20-24 are provided in the ESI.†

All data are available in the main text or the ESI.†

## Conflicts of interest

The authors declare no competing financial interest.

## Acknowledgements

This work was supported by the National Natural Science Foundation of China (Grant No. 21301057 and 22075073), Fundamental Research Funds for the Central Universities (531107051077).

## References

1 L. Zhang and Z. Chen, Polyoxometalates: tailoring metal oxides in molecular dimension toward energy applications, *Int. J. Energy Res.*, 2020, **44**, 3316–3346.
2 Y. Ji, L. Huang, J. Hu, C. Streb and Y.-F. Song, Polyoxometalate-functionalized nanocarbon materials for energy conversion, energy storage and sensor systems, *Energy Environ. Sci.*, 2015, **8**, 776–789.
3 N. I. Gumerova and A. Rompel, Synthesis, structures and applications of electron-rich polyoxometalates, *Nat. Rev. Chem.*, 2018, **2**, 0112.
4 S. J. Folkman, J. Soriano-Lopez, J. R. Galán-Mascarós and R. G. Finke, Electrochemically driven water-oxidation catalysis beginning with six exemplary cobalt polyoxometalates: Is it molecular, homogeneous catalysis or electrode-bound, heterogeneous CoOx catalysis?, *J. Am. Chem. Soc.*, 2018, **140**, 12040–12055.
5 H. Lu, J. Tournet, K. Dastafkan, Y. Liu, Y. H. Ng, S. K. Karuturi, C. Zhao and Z. Yin, Noble-metal-free multicomponent nanointegration for sustainable energy conversion, *Chem. Rev.*, 2021, **121**, 10271–10366.
6 Y. Yao, Q. Dong, A. Brozena, J. Luo, J. Miao, M. Chi, C. Wang, I. G. Kevrekidis, Z. J. Ren, J. Greeley, G. Wang, A. Anapolsky and L. Hu, High-entropy nanoparticles: Synthesis-structure-property relationships and data-driven discovery, *Science*, 2022, **376**, 3103.
7 Y. Yao, Z. Huang, P. Xie, S. D. Lacey, R. J. Jacob, H. Xie, F. Chen, A. Nie, T. Pu, M. Rehwoldt, D. Yu, M. R. Zachariah, C. Wang, R. Shahbazian-Yassar, J. Li and L. Hu, Carbothermal shock synthesis of high-entropy-alloy nanoparticles, *Science*, 2018, **359**, 1489–1494.
8 H. Xu, Z. Zhang, J. Liu, C.-L. Do-Thanh, H. Chen, S. Xu, Q. Lin, Y. Jiao, J. Wang, Y. Wang, Y. Chen and S. Dai, Entropy-stabilized single-atom Pd catalysts via high-entropy fluorite oxide supports, *Nat. Commun.*, 2020, **11**, 3908.
9 S. Chorazy, J. J. Stanek, W. Nogaś, A. M. Majcher, M. Rams, M. Kozieł, E. Juszyńska-Gałązka, K. Nakabayashi, S.-I. Ohkoshi, B. Sieklucka and R. Podgajny, Tuning of charge transfer assisted phase transition and slow magnetic relaxation functionalities in $\{Fe_{9-x}Co_x[W(CN)_8]_6\}$ (x = 0-9) molecular solid solution, *J. Am. Chem. Soc.*, 2016, **138**, 1635–1646.
10 D.-L. Long, E. Burkholder and L. Cronin, Polyoxometalate clusters, nanostructures and materials: from self assembly to designer materials and devices, *Chem. Soc. Rev.*, 2007, **36**, 105–121.
11 A. Kondinski and K. Y. Monakhov, Breaking the gordian knot in the structural chemistry of polyoxometalates: copper(II)-oxo/hydroxo clusters, *Chem. – Eur. J.*, 2017, **23**, 7841–7852.
12 M. A. Palacios, E. M. Pineda, S. Sanz, R. Inglis, M. B. Pitak, S. J. Coles, M. Evangelisti, H. Nojiri, C. Heesing, E. K. Brechin, J. Schnack and R. E. P. Winpenny, Copper keplerates: high-symmetry magnetic molecules, *ChemPhysChem*, 2016, **17**, 55–60.
13 F.-L. Liu, B. Kozlevčar, P. Strauch, G.-L. Zhuang, L.-Y. Guo, Z. Wang and D. Sun, Robust cluster building unit: icosanuclear heteropolyoxocopperate remplated by carbonate, *Chem. – Eur. J.*, 2015, **21**, 18847–18854.
14 L. Chen, J. Hu, S. S. Mal, U. Kortz, H. Jaensch, G. Mathys and R. M. Richards, Heterogeneous wheel-shaped $Cu_{20}$-polyoxotungstate $[Cu_{20}Cl(OH)_{24}(H_2O)_{12}(P_8W_{48}O_{184})]^{25-}$

 

catalyst for solvent-free aerobic oxidation of n-hexadecane, *Chem. – Eur. J.*, 2009, **15**, 7490–7497.
15 S. S. Mal and U. Kortz, The wheel-shaped $Cu_{20}$ tungstophosphate $[Cu_{20}Cl(OH)_{24}(H_2O)_{12}(P_8W_{48}O_{184})]^{25-}$ ion, *Angew. Chem., Int. Ed.*, 2005, **44**, 3777–3780.
16 G. M. Sheldrick, Crystal structure refinement with SHELXL, *Acta Cryst. C*, 2015, **71**, 3–8.
17 J. Chen, H. Zhou and F. Xu, Bottom-up self-assembly of the sphere-shaped icosametallic oxo clusters $\{Cu_{20}\}$ and $\{Cu_{12}Zn_8\}$, *Inorg. Chem.*, 2016, **55**, 4695–4697.
18 L.-C. Gui, X.-J. Wang, Q.-L. Ni, M. Wang, F.-P. Liang and H.-H. Zou, Nanospheric $[M_{20}(OH)_{12}(maleate)_{12}(Me_2NH)_{12}]^{4+}$ clusters (M = Co, Ni) with oh symmetry, *J. Am. Chem. Soc.*, 2012, **134**, 852–854.
19 Y. Xu, N. A. Vermeulen, Y. Liu, J. T. Hupp and O. K. Farha, SALE-Ing a MOF-Based "Ship of Theseus". Sequential Building-Block Replacement for Complete Reformulation of a Pillared-Paddlewheel Metal-Organic Framework, *Eur. J. Inorg. Chem.*, 2016, **2016**, 4345–4348.
20 M. Manoli, S. Alexandrou, L. Pham, G. Lorusso, W. Wernsdorfer, M. Evangelisti, G. Christou and A. J. Tasiopoulos, Magnetic "molecular oligomers" based on decametallic supertetrahedra: a giant $Mn_{49}$ cuboctahedron and its $Mn_{25}Na_4$ fragment, *Angew. Chem., Int. Ed.*, 2016, **55**, 679–684.
21 A. Amiri and R. Shahbazian-Yassar, Recent progress of high-entropy materials for energy storage and conversion, *J. Mater. Chem. A*, 2021, **9**, 782–823.
22 A. Sarkar, Q. Wang, A. Schiele, M. R. Chellali, S. S. Bhattacharya, D. Wang, T. Brezesinski, H. Hahn, L. Velasco and B. Breitung, High-Entropy Oxides: Fundamental Aspects and Electrochemical Properties, *Adv. Mater.*, 2019, **31**, 1806236.
23 Y. Jien-Wei, C. Swe-Kai, G. Jon-Yiew, L. Su-Jien, C. Tsung-Shune, S. Tao-Tsung, C.-H. Tsau and S.-Y. Chang, Formation of simple crystal structures in Cu-Co-Ni-Cr-Al-Fe-Ti-V alloys with multiprincipal metallic elements, *Metall. Mater. Trans. A*, 2004, **38**, 2533–2536.
24 H. Irving and R. Williams, The stability of transition-metal complexes, *J. Chem. Soc.*, 1953, 3192–3210.
25 J.-W. Zhao, Y.-Z. Li, L.-J. Chen and G.-Y. Yang, Research progress on polyoxometalate-based transition-metal-rare-earth heterometallic derived materials: synthetic strategies, structural overview and functional applications, *Chem. Commun.*, 2016, **52**, 4418–4445.
26 D. Li, P. Ma, J. Niu and J. Wang, Recent advances in transition-metal-containing Keggin-type polyoxometalate-based coordination polymers, *Coord. Chem. Rev.*, 2019, **392**, 49–80.
27 S.-S. Wang and G.-Y. Yang, Recent advances in polyoxometalate-catalyzed reactions, *Chem. Rev.*, 2015, **115**, 4893–4962.
28 J. Zhang, H. Wang, L. Wang, S. Ali, C. Wang, L. Wang, X. Meng, B. Li, D. S. Su and F.-S. Xiao, Wet-chemistry strong metal-support interactions in titania-supported Au catalysts, *J. Am. Chem. Soc.*, 2019, **141**, 2975–2983.
29 L. Liu and A. Corma, Metal catalysts for heterogeneous catalysis: from single atoms to nanoclusters and nanoparticles, *Chem. Rev.*, 2018, **118**, 4981–5079.
30 X. Wang, S. Song and H. Zhang, A redox interaction-engaged strategy for multicomponent nanomaterials, *Chem. Soc. Rev.*, 2020, **49**, 736–764.
31 X.-H. Xia, Z.-J. Jia, Y. Yu, Y. Liang, Z. Wang and L.-L. Ma, Preparation of multi-walled carbon nanotube supported $TiO_2$ and its photocatalytic activity in the reduction of $CO_2$ with $H_2O$, *Carbon*, 2007, **45**, 717–721.
32 K. Mori, N. Hashimoto, N. Kamiuchi, H. Yoshida, H. Kobayashi and H. Yamashita, Hydrogen spillover-driven synthesis of high-entropy alloy nanoparticles as a robust catalyst for $CO_2$ hydrogenation, *Nat. Commun.*, 2021, **12**, 1–11.
33 X. Cui, P. Xiao, J. Wang, M. Zhou, W. Guo, Y. Yang, Y. He, Z. Wang, Y. Yang and Y. Zhang, Highly branched metal alloy networks with superior activities for the methanol oxidation reaction, *Angew. Chem.*, 2017, **129**, 4559–4564.
34 G. Rajeshkhanna and G. Ranga Rao, Micro and nano-architectures of $Co_3O_4$ on Ni foam for electro-oxidation of methanol, *Int. J. Hydrogen Energy*, 2018, **43**, 4706–4715.
35 L. Qian, L. Gu, L. Yang, H. Yuan and D. Xiao, Direct growth of $NiCo_2O_4$ nanostructures on conductive substrates with enhanced electrocatalytic activity and stability for methanol oxidation, *Nanoscale*, 2013, **5**, 7388–7396.
36 Y. Sun, Y. Zhou, C. Zhu, W. Tu, H. Wang, H. Huang, Y. Liu, M. Shao, J. Zhong, S.-T. Lee and Z. Kang, Synergistic Cu@CoOx core-cage structure on carbon layers as highly active and durable electrocatalysts for methanol oxidation, *Appl. Catal., B*, 2019, **244**, 795–801.
37 W.-D. Hsu, M. Ichihashi, T. Kondow and S. B. Sinnott, Ab Initio Molecular Dynamics Study of Methanol Adsorption on Copper Clusters, *J. Phys. Chem. A*, 2007, **111**, 441–449.
38 Y. Tong, X. Yan, J. Liang and S. X. Dou, Metal-Based Electrocatalysts for Methanol Electro-Oxidation: Progress, Opportunities, and Challenges, *Small*, 2021, **17**, 1904126.
39 S. Anantharaj, H. Sugime and S. Noda, Ultrafast Growth of a $Cu(OH)_2$-CuO Nanoneedle Array on Cu Foil for Methanol Oxidation Electrocatalysis, *ACS Appl. Mater. Interfaces*, 2020, **12**, 27327–27338.
40 F. Chen, N. Wu, M. Zhai, X. Zhang, R. Guo, T. Hu and M. Ma, Robust copper nanocrystal/nitrogen-doped carbon monoliths as carbon monoxide-resistant electrodes for methanol oxidation reaction, *J. Energy Chem.*, 2021, **58**, 247–255.
41 S. Anantharaj, H. Sugime, S. Yamaoka and S. Noda, Pushing the limits of rapid anodic growth of $CuO/Cu(OH)_2$ nanoneedles on Cu for the methanol oxidation reaction: anodization pH is the game changer, *ACS Appl. Energy Mater.*, 2021, **4**, 899–912.
42 S. M. Pawar, B. S. Pawar, A. I. Inamdar, J. Kim, Y. Jo, S. Cho, S. S. Mali, C. K. Hong, J. Kwak, H. Kim and H. Im, *In situ* synthesis of $Cu(OH)_2$ and CuO nanowire electrocatalysts for methanol electro-oxidation, *Mater. Lett.*, 2017, **187**, 60–63.